High-speed IPM Motors with Rotor Sleeve: Structural Design and Performance Evaluation

High-speed IPM Motors with Rotor Sleeve: Structural Design and Performance Evaluation

Josef Binder
Technical University of Darmstadt
Darmstadt, Germany
josef.binder@stud.tu-darmstadt.de

Mario Silvagni
Department of Mechanical and Aerospace Engineering
Politecnico di Torino
Turin, Italy
mario.silvagni@polito.it

Simone Ferrari
Department of Energy
Politecnico di Torino
Turin, Italy
simone.ferrari@polito.it

Björn Deusinger
Institute of Electrical Energy Conversion
Technical University of Darmstadt
Darmstadt, Germany
bjoern.deusinger@tu-darmstadt.de

Andrea Tonoli
Department of Mechanical and Aerospace Engineering
Politecnico di Torino
Turin, Italy
andrea.tonoli@polito.it

Gianmario Pellegrino
Department of Energy
Politecnico di Torino
Turin, Italy
gianmario.pellegrino@polito.it

***Abstract* — This paper deals with the structural design of sleeves for high-speed interior permanent magnet (IPM) synchronous machines. Wrapped IPM (WIPM) motors are a new player in the field of high-speed e-machines for traction, where a retaining sleeve is used to hold the magnetic poles in place against centrifugal forces, replacing the role of conventional iron bridges. The wrapping technique, originating from surface-mounted permanent magnet rotors, is believed to push speed limitations to new heights, as demanded by the increasing requirements of the automotive industry. By developing an equivalent rotor geometry of the WIPM rotor, an analytical model is formulated to evaluate the stress in the rotor and to provide a quick and intuitive tool for the sleeve design. The results are successfully validated by structural finite element analysis. Also, the output figures of a WIPM machine are compared to those of an equivalent IPM machine with iron bridges.**

Keywords—interior permanent magnet (IPM) synchronous machine, rotor retaining sleeve, centrifugal stress, carbon fiber, electric motor design, high-speed electric motor, analytical method, finite element analysis (FEA)

I. Introduction

The majority of drivetrains in commercially available electric vehicles uses magnet-less induction motors or synchronous motors with interior permanent magnets (IPM) excitation [1, 2]. A popular example is shown in Fig. 1-a. The structural integrity of such IPM rotors relies on the strength of the rotor lamination steel. Thin iron connections, mostly referred to as bridges or ribs, cross the PM housing pockets and retain the magnets and the rotor poles themselves against centrifugal forces due to rotation. The thickness of the ribs is to be designed according to the desired maximum speed, at which the mechanical stress in the ribs must stay below a prescribed stress limit – thicker bridges allow higher speeds. However, to avoid substantial magnetic stray flux through the bridges, they also need to be designed as thin as possible. An ideal design regarding the reduction of bridge leakage flux would have ribs of zero thickness. Time-consuming and computation-intensive structural finite element analysis (FEA) is usually required to obtain a rib design that ensures both safe operation and minimum stray flux in the ribs.

In 2021, a new design for IPM rotors has been presented by the electric car manufacturer Tesla as a patent [3] and as a market product on board of the company's vehicle Model S Plaid. All iron ribs are removed, resulting in loose outer poles of electrical steel sited on the PMs in the flux barrier. Instead, a prestressed sleeve is placed over the rotor to retain the PMs and the pole pieces. This is shown in principle in Fig. 1-b and is subsequently named wrapped IPM (WIPM) motor. Tesla claims to achieve better efficiency and flux utilization as well as higher torque and power at the same speeds compared to conventional PM machines with the same PM mass [3].

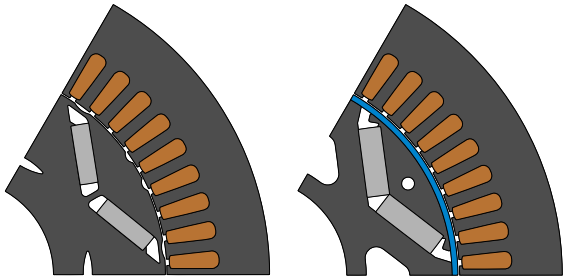

a) Tesla Model 3 b) Tesla Model S Plaid

Fig. 1. Examples of a conventional IPM motor a) and a WIPM motor b) with a only a single machine pole depicted.

Rotor retaining sleeves for electrical machines have been comprehensively investigated and used in surface-mounted PM (SPM) synchronous motor topologies, especially in applications demanding high speeds at which conventional IPM designs are impractical and/or inefficient. The simple layered SPM structure allows for an analytical design of the sleeve thickness which mainly determines the maximum allowable rotor speed [4]. The applied sleeve materials include nonmetallic composites such as glass fiber or carbon fiber (CF) [4] and metals such as titanium alloys [5] or copper [6], sometimes combined within several sleeve layers. Typical mounting methods for the sleeve are shrink-fitting [7] and press-fitting [8]. Tesla on the other hand is using a pretensioned filament winding of CF with epoxy resin that is applied directly onto the rotor in circumferential direction. This technique has been investigated for example in [9].

This paper presents an analytical approach to preliminarily design a wrapping for a WIPM rotor by calculating the stress in the sleeve under prestress, rotation, and temperature load. The analytical results are then validated by structural FEA and a sleeve thickness design procedure is proposed. The

WIPM motor performance is compared to the one of an equivalent IPM machine with structural rotor bridges. The work presented is implemented as MATLAB code into the open-source motor design and analysis platform SyR-e [10]. The software COMSOL Multiphysics was used for the validation by structural FEA.

II. Analytical Model

Preventing the PMs from detaching from the rotor back-iron during operation is the main sleeve design condition, which may be fulfilled by a sufficient prestressing of the wrapping. To avoid its failure, the sleeve thickness is to be chosen so that the sleeve stress stays below a prescribed stress limit.

A. Simplified Equivalent Geometry

To analytically evaluate these conditions, the WIPM rotor geometry is simplified into a layered disk model as shown in Fig. 2. The sleeve is kept unchanged. All loose masses, i. e. the pole pieces and PMs, that would detach from the rotor once rotating without a wrapping, are summarized into a single ring segment. This is motivated by the assumption of no relative motion between PMs and pole piece and their single solid body behavior, as long as the wrapping is compressing both against the back-iron. The equivalent ring's mass density ρ and its elastic properties depend on the properties of the PMs and pole piece. First, the Young's modulus E and Poisson's ratio ν of the pole piece are estimated considering the influence of its hole [11]. Then, applying the "rule of mixture" and "inverse rule of mixture" [12], ρ, E, ν, and the thermal expansion coefficient α of the equivalent ring segment are approximated. The back-iron is simplified into a ring with unchanged material characteristics and serves as a counterpart for the sleeve prestress.

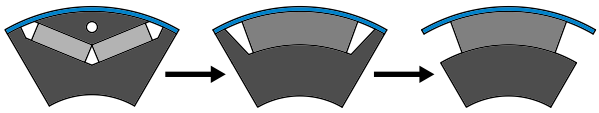

Fig. 2. Concept of the transformation from the WIPM geometry to an equivalent rotor consisting of two rings and loose ring segments in between.

The sleeve is labeled with subscript 1, the combined ring segment of PMs and pole piece with 2, and the back-iron with 3. The layer outer and inner radii are defined as shown in Fig. 3, where $r_{1i} = r_{2o}$ and $r_{2i} = r_{3o}$.

B. Stress Analysis

Assuming a plane stress state and exploiting the axisymmetry in a polar coordinate system, the normal stresses σ_r, σ_t and strains ε_r, ε_t of each continuous disk layer in radial (subscript r) and circumferential (t) direction can be described by the radial coordinate r alone. Including thermal expansion with a temperature rise ΔT, Hooke's law for a homogeneous and isotropic material links stresses and strains by (1) [13]:

$$\begin{pmatrix} \varepsilon_r \\ \varepsilon_t \end{pmatrix} = \begin{pmatrix} 1/E & -\nu/E \\ -\nu/E & 1/E \end{pmatrix} \begin{pmatrix} \sigma_r \\ \sigma_t \end{pmatrix} + \alpha \Delta T \begin{pmatrix} 1 \\ 1 \end{pmatrix} \tag{1}$$

For composites such as CF with orthotropic material behavior as a circumferentially wound sleeve, the assumption of isotropy is not true. However, the accuracy improvement of an orthotropic sleeve model does not justify the increase in complexity compared to isotropic modeling [8].

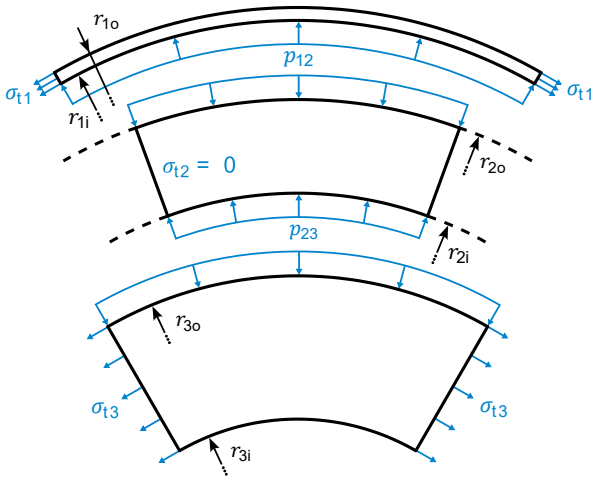

Fig. 3. Radii, stresses, and contact pressures in the equivalent rotor.

Assuming constant mechanical angular speed ω_m, shear stress and strain are negligible. Introducing the radial displacement u linked to the strains by (2) and (3), the specialized solving differential equation (4) as a basis for the analytical stress model is formulated [13]. Its right side represents the centrifugal load.

$$\varepsilon_r = \mathrm{d}u/\mathrm{d}r \tag{2}$$

$$\varepsilon_t = u/r \tag{3}$$

$$\frac{\mathrm{d}^2u}{\mathrm{d}r^2} + \frac{1}{r}\frac{\mathrm{d}u}{\mathrm{d}r} - \frac{u}{r^2} = -(1-\nu^2)\frac{\rho\omega_m^2 r}{E} \tag{4}$$

Solving (4) for both the homogeneous and particular solution by integrating the left side twice results in an expression for u containing two integration constants. Inserting u into (2) and (3) and the results into (1) yields expressions for the radial stress σ_r and circumferential stress σ_t.
The integration constants are found by imposing boundary conditions (5) and (6) on the radial stress that represent surface forces: a contact pressure p_o on the outer radius and p_i on the inner radius of the disk.

$$\sigma_r(r_o) = -p_o \tag{5}$$

$$\sigma_r(r_i) = -p_i \tag{6}$$

The resulting solutions for the stresses and displacement in a single continuous layer can be found in [13].
Since the segmented middle layer is not a continuous disk, its equations are derived in another way. This paper applies the approach used in [14] and therefore simplifies with (7):

$$\sigma_{t2}(r) = 0 \tag{7}$$

The remaining expressions for only σ_{r2} and u_2 again contain two integration constants solved for by two boundary conditions. Simplification (7) is justified by the second rotor layer being split into circumferentially distributed pieces that are disconnected from each other. Therefore, circumferential stress cannot be transmitted. Any information on the circumferential span of each segment is lost, as indicated in Fig. 3 by the dashed line continuation of the second layer.

With simplification (8) presented in [4], the 3-layer system can be reduced by another equation: as the designed sleeves are thin compared to their diameter, the radial sleeve stress σ_{r1} is negligible. Both σ_{t1} and u_1 become independent of r, and r_{1i} and r_{1o} are reduced to the average sleeve radius $r_{1,av}$. Only one integration constant obtained through the inner contact pressure p_{12} remains, while we assume zero contact pressure on the outside of the wrapping.

$$\sigma_{r1}(r) = 0 \tag{8}$$

C. Condition 1: Assembly Under Compression

As long as the sleeve compresses the assembly, (9)-(12) describe the couplings:

$$\sigma_{r2}(r_{2o}) = -p_{12} \tag{9}$$

$$\sigma_{r2}(r_{2i}) - \sigma_{r3}(r_{3o}) = 0 \tag{10}$$

$$u_1 - u_2(r_{2o}) = \Delta u_{12} \tag{11}$$

$$u_2(r_{2i}) - u_3(r_{3o}) = 0 \tag{12}$$

Conditions (9) and (10) are obtained from the equality of radial stresses between layer 1 and 2 as well as between layer 2 and 3. Condition (11) considers an interference fit with the assembly interference Δu_{12} at the interface radius $r_{1i} = r_{2o}$, resulting in a prestressing of the sleeve. Condition (12) states that there is no interference between the second layer and the back-iron.

D. Condition 2: PM Lift-off

Above a certain speed, the prestress of the wrapping is not sufficient anymore to fix the pole pieces and PMs to the back-iron against the centrifugal forces. It is furthermore referred to as the lift-off speed $\omega_{m,off}$, and is defined as the speed at which the contact pressure p_{23} becomes zero, i. e. when the PMs detach from the back-iron.

Then, the boundary conditions (10) and (12) need to be adapted to (13) and (14), now describing the decoupling of the first two layers from the rotor back-iron:

$$\sigma_{r2}(r_{2i}) = 0 \tag{13}$$

$$p_{23} = 0 \tag{14}$$

The approach described until here particularly allows to calculate the circumferential sleeve stress σ_{t1} and the lift-off speed $\omega_{m,off}$.

III. Finite Element Model

Structural FEA is used to validate the analytical approach described previously and enables the evaluation of the actual WIPM rotor geometry without the simplifications adopted for the analytical model. Additional effects, such as bending of the sleeve or nonuniform contact pressures between components, can be considered. This however could come at the cost of time-consuming modeling and computation, wherefore a sleeve design by FEA should be used for the refinement of the analytical design estimation.

The structural FEA models used in this paper (Fig. 4) represent single rotor poles of 60° mechanical circumferential span drawn in a 2D cross-sectional plane Their dimensions are motivated by the WIPM motor of the Tesla Model S Plaid. Symmetry boundary conditions are applied on the pole sides. All materials are modeled homogeneous and isotropic to be compliant with the analytical model assumptions and for an easier FEA computation. The loads considered are the centrifugal force and the sleeve prestressing through an interference fit. Thermal expansion, the magnetic force of the PMs and friction effects are neglected. All contact surfaces between the different components contain contact elements for the evaluation of the contact pressures along the interface surfaces. They also enable the detachment of the coupled components. This feature is complemented by spring foundation constraints that prevent loose components from entering an undefined state.

The four models seen in Fig. 4 were created for different objectives: model A reflects the geometry used in the analytical approach and is used for its validation. The segmentation of the middle layer is accounted for by two segments separated by a 0.5° circumferential gap between them to prevent the transmission of circumferential stress.

Models B-D directly simulate the WIPM rotor geometry. The prestressed wrapping will bend over the flux barrier gap, therefore the influence of bending on the sleeve stress will be visible in all three models. The addition of air pockets in model C and the extension of the pole piece sides in model D, both motivated by the same structures as in the Tesla Model S Plaid WIPM rotor, allow for the investigation of their influence on the sleeve stress and PM lift-off speed.

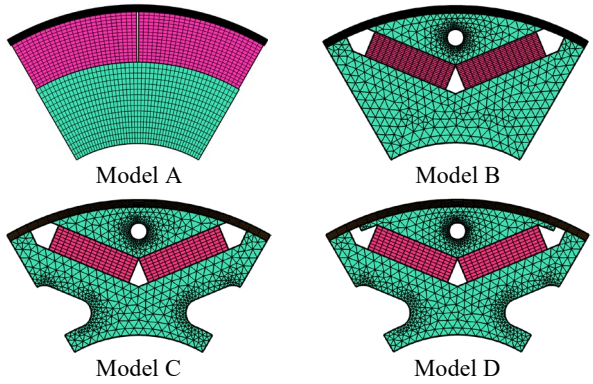

Fig. 4. Structural FEA models created for this paper. Model A is used to validate the analytical model, while the others serve the evaluation of the actual WIPM geometry, with increasing level of detail from model B to D.

A. FEA Validation of the Simplified Analytical Model

First, the analytical model is validated with FEA model A. The applied properties are summarized in Table I, which also contains the properties of the 2nd layer ring segment in the analytical model.

Fig. 5 shows the results for an assembly interference of $\Delta u_{12} = 0.1$ mm. The analytical model comparison yields satisfying results. Despite simplification (8), the model is able to indirectly calculate the correct maximum radial sleeve stress from the contact pressure at r_{1i} with $\sigma_{r1}(r_{1i}) = -p_{12}$. The PM lift-off occurs when $\sigma_{r2}(r_{2i}) = -p_{23} = 0$ in the second plot. Afterwards, the sleeve circumferential stress and the contact pressure p_{12} increase sharply proportional ω_m^2, so the lift-off

point can be fixed to when the inclination of the sleeve stress suddenly increases. The operating state of detached PMs is prohibited. Therefore, the maximum allowable speed is $\omega_{m,off}$ or below, if a safety margin is applied.

TABLE I. MATERIAL PROPERTIES

	Sleeve DW236 (Circomp GmbH)	*PMs BMN-52UH*	*Electric steel M270-35A*	*2nd layer ring segment*
E	175 GPa	175 GPa	200 GPa	170.4 GPa
ν	0.28	0.24	0.3	0.261
ρ	1550 kg/m³	7550 kg/m³	7650 kg/m³	7511 kg/m³

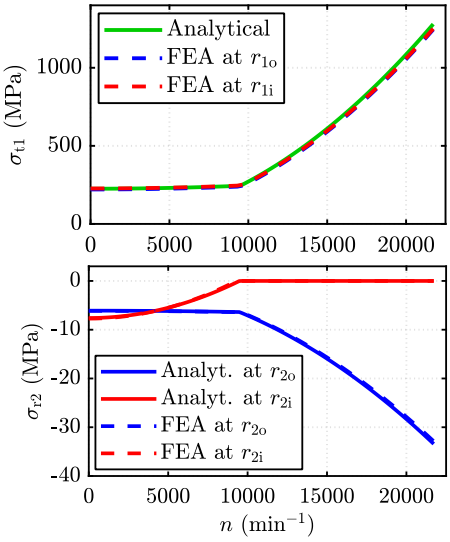

Fig. 5. Circumferential sleeve stress and 2nd layer radial stress in the analytical model and FEA model A for $\Delta u_{12} = 0.1$ mm and $\Delta T = 0$ K.

B. Comparative FEA Results

A comparison of the sleeve stress in models B, C and D for a wrapping of 2 mm thickness and three different assembly interferences Δu_{12} is shown in Fig. 6; stress is taken in the middle of the pole piece at the outer sleeve radius r_{1o}. Since σ_{r1} is zero at r_{1o}, only the circumferential stress is present. Taking the stress value outside of areas affected by bending also later ensures comparability to the analytical model.

All three models show similar behavior as in Fig. 5. Further, we see that larger values of Δu_{12} lead to larger sleeve prestress, which the sleeve must endure together with the smaller increase due to the centrifugal load. The lift-off speeds increase with larger prestress, enabling higher speeds. The addition of air pockets in models C and D lowers the sleeve stress by 2.9 % compared to model B for all three interferences. This results from the pockets reducing the inner rotor structure stiffness, which reduces its resistance against the prestress of the sleeve. Approaching the lift-off speed, the influence of the lowered stiffness gradually vanishes and the error decreases to neglectable values below 0.13 %.

When adding the pole piece extensions (model D), the stress only increases by less than 0.7 % with respect to model C. Regarding the lift-off speed, model D calculates it to be 0.3 % larger compared to model B, while there is no detectable difference in $\omega_{m,off}$ between C and D.

We conclude that the simplified FEA model B is sufficient for validating the analytical design of a WIPM rotor. Sleeve bending and edge effects however need to be examined separately in more detailed models during design refinement.

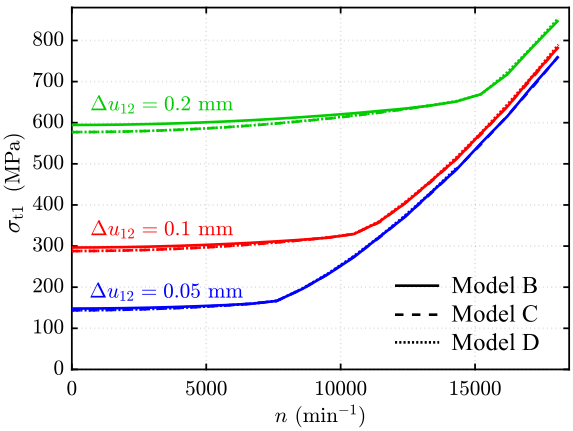

Fig. 6. Comparison of the computed sleeve circumferential stress over the rotor speed in WIPM rotor FEA models B, C, and D for different assembly interferences. (The comparison was carried out with a different set of material properties than given in Table I.)

IV. SLEEVE DESIGN FOR WIPM MOTORS

A structurally optimal sleeve design utilizes its capability to withstand stress as much as possible, while keeping its thickness minimum to avoid unnecessary increase of the magnetic air gap, sum of the mechanical air gap and the nonmagnetic sleeve. This section aims to provide a simple procedure to design a sleeve of minimum thickness for a given WIPM rotor geometry and a target maximum speed.

A. Accuracy of the Analytical Model Design

First, the circumferential sleeve stress in the analytical model and FEA model B is compared for various assembly interferences in Fig. 7 The sleeve thickness of 2 mm is kept constant, and no temperature load is applied.

Comparing on the outer sleeve radius r_{1o} before lift-off, we find that the analytical model calculates the sleeve stress with an overestimate of 2.5 % with respect to the FEA solution for all five prestress conditions. Considering the stress being maximum on the inner sleeve radius r_{i1}, the error there is a 1.3 % underestimate or less, depending on the prestress. In FEA, the sleeve, pole piece, and PMs are able to bend, leading to a gradual loss of contact. Referring to the lift-off speed, the analytical model overestimates it by less than 8.6 % with respect to FEA. In conclusion, the analytical model yields satisfactory results for the sleeve stress, while the actual lift-off speed is slightly overestimated.

B. Sleeve Thickness Design Procedure

A key aspect in the analytical results in Fig. 7 is that all points of PM detachment for a single sleeve thickness are summarized by the sleeve stress parabola with zero prestress. The FEA solution shows similar behavior with slightly lower lift-off speed values.

To find an optimal sleeve thickness design procedure, the influence of varying sleeve thickness and operating temperature is examined. Fig. 8 shows that thicker sleeves lead to flatter stress parabolas. Further, an overall rotor temperature increase ($\Delta T = 120$ K in Fig. 8) increases the sleeve stress by a fixed portion. This portion is neither dependent on the speed nor the assembly interference. For example, the difference is taken between the graphs with only

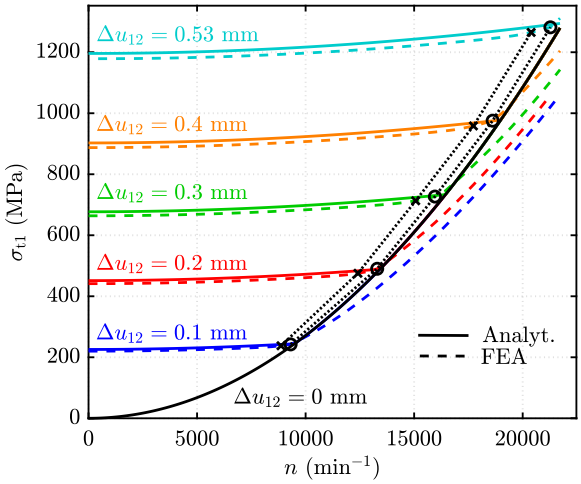

Fig. 7. Circumferential sleeve stress in the analytical model compared to FEA model B for zero temperature rise and various prestresses. "X" indicates the beginning and "O" the end of the PM detachment in the FEA model.

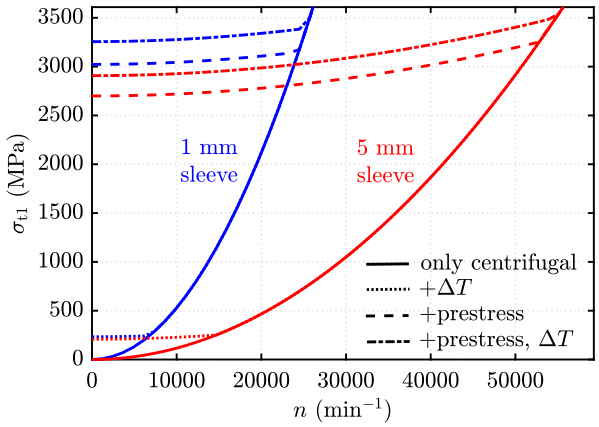

Fig. 8. Circumferential sleeve stress behavior under various load type conditions for two different sleeve thicknesses.

the assembly interference considered (here 1.3 mm) to the graphs with both the interference and the temperature load considered. The difference stays constant independently of the speed. Further, this difference is equal to the offset prestress with only the temperature load applied, when both the speed and the assembly interference are zero.

A structurally optimal sleeve design is found, if the sleeve stress at the lift-off speed added by the stress increase $\sigma_{\Delta T}$ from the temperature load equals the maximum allowable stress $\sigma_{t1,max}$. In the stress vs. speed plane (Fig. 9), the found optimal sleeve thickness points for the respective maximum operating speed are marked by "X". First, the desired maximum speed is chosen. Then, the optimal sleeve thickness is found by vertically intersecting the red graph connecting all optimal sleeve design points. Precalculating this optimal design curve allows to swiftly find the minimum sleeve thickness for a target maximum speed as the input. The required assembly interference can be then calculated by solving the analytical model for Δu_{12} once the sleeve thickness has been obtained.

Fig. 9 gives an example. For sleeves from 0.3 to 4 mm thickness, the added thermal stress reaches from 238 to 214 MPa, forming the red curve. It is $\sigma_{t1,max}$ = 1680 MPa, if a safety factor of 2 is applied to the sleeve DW236. Assume that the desired maximum speed is set at 20150 min^{-1} without any margin to the lift-off speed. At this speed, a 1.5 mm thick sleeve would reach $\sigma_{t1,max}$ if heated up with 120 K. During cold operation, this speed is equal to the lift-off speed n_{off}, and the sleeve stress would follow the dashed green line for speeds below n_{off}, down to a prestress of 1363 MPa. The analytical model calculates the necessary assembly interference to Δu_{12} = 0.595 mm.

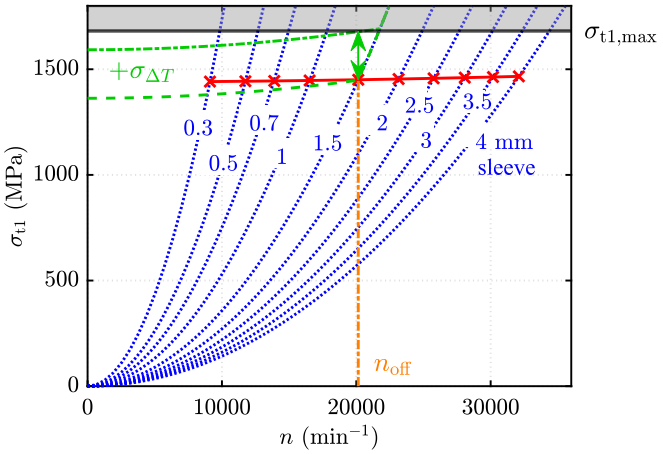

Fig. 9. Minimum sleeve thickness designs, given by the red curve.

V. Comparative Motor Performance Evaluation

In this section, the performances of a conventional IPM motor and of a WIPM motor are compared. The traction motors chosen are of the Tesla Model 3 and Model S Plaid (Fig. 1). Both motors have the same stator. In the comparison, the electrical rating (Table II) and the materials of the rotor (Table I) are assumed identical, excluding the CF sleeve of the Model S Plaid. Its thickness is estimated to be 2 mm to the authors' knowledge. The maximum operational speed of the motors is 18100 min^{-1}, with an overspeed set at least at 20000 min^{-1}. Further, operating temperatures of 80 °C for the PMs and 100 °C for the stator windings are assumed. SyR-e [10] was used to obtain all results by means of FEA.

The flux linkage curves of the two motors are shown and compared in Fig.10. The open circuit PM flux linkage is 0.067 Vs for the Model 3 and 0.072 Vs for Model S Plaid, with the slight advantage of the latter relating to the absence of rotor ribs. Moreover, the slope of the flux linkage curves in the S Plaid case is gentler for both axes due to the larger magnetic airgap (2.7 mm vs. 0.7 mm). The torque vs. ampere curves under maximum torque per ampere (MTPA) conditions are well matched in Fig. 11, although the two motors have a different mix of PM and reluctance torque: higher PM torque for the Model S Plaid and lower reluctance

TABLE II. Tesla Model 3 and Model S Plaid Data

Max. current	I_{max}	1404	[Apk]
Max. current density	J_{max}	36	[Apk/mm^2]
DC link voltage	V_{dc}	231	[V]
Stator outer diameter	D	225	[mm]
Rotor outer diameter	d	149.9	[mm]
Mechanical air gap	g	0.7	[mm]
Stack length	L	134	[mm]
Sleeve thickness (S Plaid)	h_{sl}	2	[mm]

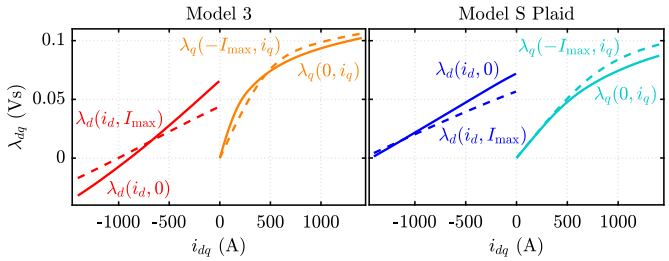

Fig. 10. Flux linkage maps of the Tesla Model 3 and S Plaid compared.

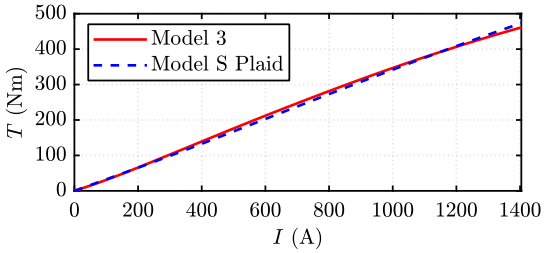

Fig. 11. Comparison of MTPA torque vs. peak current up to rated current.

torque for same total torque. The aggregate of a larger PM flux linkage and a milder d-axis flux linkage rate of change reflects into a larger characteristic current for the Model S Plaid: 1443 A versus 896 A in the Model 3, visible from the saturation curves as the intercept of $\lambda_d(i_d,0)$ with 0 Vs. A flat power curve at high operating speed and maximum current is thus expected for the Model S Plaid motor drive, having a characteristic current close to the current rating of 1404 A, whereas lower power at high speed is expected from the Model 3 motor due to its lower characteristic current [15].

The superior flux weakening capability of the Model S Plaid is evident in Fig. 12. Below the base speed, the two motors have similar torque, but the better characteristic to maximum current ratio of the Model S Plaid results in a constant power speed range at almost 266 kW, while Model 3 reaches a peak of 217 kW declining to 176 kW at maximum speed.

Summarizing, the S Plaid motor dominates in most aspects, with its main advantage of a flat power curve with 51 % greater power at maximum speed. However, it uses 43 % more PM material compared to the Model 3. If the torque and power vs. PM mass ratios are compared, the Model 3 is the more PM material saving motor. Related to the overall rotor mass instead, the S Plaid with its lightweight sleeve and less electric steel achieves greater power and torque density.

VI. Conclusion and Prospect

This paper proposed an analytical model to calculate the sleeve stresses and maximum feasible operating speed in novel WIPM motors. The model was validated by structural FEA, excluding thermal expansion effects. A preliminary analytical design approach to quickly find the minimum sleeve thickness for a target maximum speed was suggested then. Finally, a performance analysis between an IPM and a WIPM motor illustrated advantages of the new rotor type.

However, more comparative studies, e. g. between WIPM and IPM motors having the same PM mass, are necessary to conclude under which circumstances and for which design decisions WIPM machines are advantageous compared to conventional PM synchronous motors.

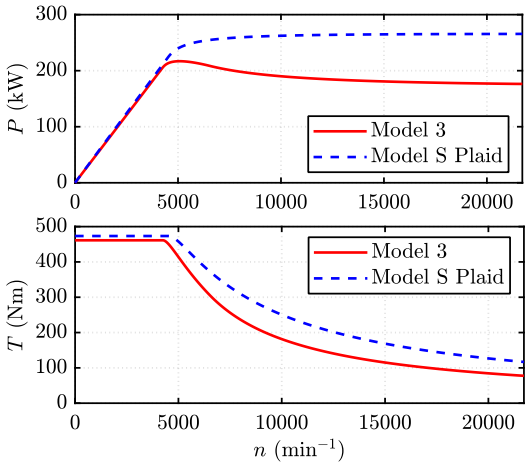

Fig. 12. Comparison of power and torque vs. speed.

References

[1] C. S. Goli, M. Manjrekar, S. Essakiappan, P. Sahu, and N. Shah, "Landscaping and Review of Traction Motors for Electric Vehicle Applications," *2021 IEEE Transportation Electrification Conference & Expo (ITEC)*, Chicago, IL, USA, 2021, pp. 162–168.

[2] Z. Wang, T. W. Ching, S. Huang, H. Wang, and T. Xu, "Challenges Faced by Electric Vehicle Motors and Their Solutions," *IEEE Access*, vol. 9, pp. 5228–5249, 2021.

[3] L. E. Olsen, *et al.*, "Permanent magnet motor with wrapping", WO2021225902 (A1), Nov 11, 2021.

[4] A. Binder, T. Schneider, and M. Klohr, "Fixation of buried and surface-mounted magnets in high-speed permanent-magnet synchronous machines," *IEEE Trans. on Ind. Applicat.*, vol. 42, no. 4, pp. 1031–1037, 2006.

[5] F. Zhang, G. Du, T. Wang, G. Liu, and W. Cao, "Rotor Retaining Sleeve Design for a 1.12-MW High-Speed PM Machine," *IEEE Trans. on Ind. Applicat.*, vol. 51, no. 5, pp. 3675–3685, 2015.

[6] H. Fang, D. Li, R. Qu, J. Li, C. Wang, and B. Song, "Rotor Design and Eddy-Current Loss Suppression for High-Speed Machines With a Solid-PM Rotor," *IEEE Trans. on Ind. Applicat.*, vol. 55, no. 1, pp. 448–457, 2019.

[7] X. Li, N. Erd, and A. Binder, "Design and calculation of a 130 kW high-speed permanent magnet synchronous machine in flywheel energy storage systems for urban railway application," in *2017 6th International Conference on Clean Electrical Power (ICCEP)*, Santa Margherita Ligure, Italy, Jun. 2017, pp. 452–459.

[8] H. Polinder, J. A. Ferreira, and A. Borisavljevic, "Enclosure design for a high-speed permanent magnet rotor," in *5th IET International Conference on Power Electronics, Machines and Drives (PEMD 2010)*, Brighton, UK, Apr. 2010, p. 416–421.

[9] L. Zu, H. Xu, B. Zhang, D. Li, H. Wang, and B. Zi, "Filament-wound composite sleeves of permanent magnet motor rotors with ultra-high fiber tension," *Composite Structures*, vol. 204, pp. 525–535, 2018.

[10] S. Ferrari and G. Pellegrino, "SyR-e." Accessed: Jan. 17, 2023. [Online]. Available: https://github.com/SyR-e.

[11] I. Tsukrov and J. Novak, "Effective elastic properties of solids with defects of irregular shapes," *International Journal of Solids and Structures*, vol. 39, no. 6, pp. 1539–1555, 2002.

[12] S. Zhao, *et al.*, "Functionally graded graphene reinforced composite structures: A review," *Engineering Structures*, vol. 210, 2020.

[13] V. Vullo and F. Vivio, Rotors: Stress Analysis and Design, 1st ed. Milano: Springer Milan, 2013.

[14] W. Cheng, Z. Deng, L. Xiao, B. Zhong, and B. Zhang, "Strength analytical solution to ultra-high-speed permanent magnet rotor considering temperature gradient and segmental permanent magnet effect," *Advances in Mechanical Engineering*, vol. 11, no. 4, 2019.

[15] W. L. Soong and T. J. E. Miller, "Field-weakening performance of brushless synchronous AC motor drives," *IEE Proc., Electr. Power Appl.*, vol. 141, no. 6, p. 331, 1994.